# Synthesis, investigation, structural and elastic properties of Mg$_x$Zn$_{1-x}$Fe$_2$O$_4$ nanoparticles

Pradip V. Patil[1,a], Nandkishor D. Chaudhari[2,b], Prabhakar R. Kute[2,c], Rajendra D. Kale[3,d]

[1]PG Department of Physics and Research Centre, VP's ASC College Baramati (Pune), 413133, India

[2]Department of Physics and Chemistry, Pratishthan Mahavidyalaya, Paithan (Aurangabad), 431107, India

[3]Department of Physics, Tuljaram Chaturchand College, Baramati (Pune), 413102, India

[a]vpasccphysics@gmail.com, [b]nk.dchaudhari@gmail.com, [c]kuteprabhakar@gmail.com, [d]rajendra_kale@yahoo.com

Corresponding author: Rajendra D. Kale, rajendra_kale@yahoo.com

ABSTRACT  Magnesium-Zinc Ferrite nanoparticles of different compositions are synthesized by using the sol-gel auto-combustion method with citric acid as a fuel. Structural characteristics were studied using X-ray diffraction technique and it confirms the formation of cubic spinel structure. The ferrite nanoparticle size of synthesized powder ranges from 22 – 24 nm. The effect of change in Mg$^{2+}$ content results in a change of the lattice parameter of ferrite nanoparticles. In the present paper, the structural parameters such as cation-cation and cation-anion distances, tetrahedral, octahedral bond lengths and bond angles, hopping lengths, shared, unshared tetrahedral, and octahedral edge are reported. FTIR spectra show two prominent peaks around 524 – 532 cm$^{-1}$ (tetrahedral site) and 409 – 432 cm$^{-1}$ (octahedral site) and the force constants of the octahedral and tetrahedral site of Mg–Zn ferrite were calculated. The elastic moduli and other factors such as longitudinal, transverse and mean velocity, Poisson ratio, and Debye temperature were determined.

KEYWORDS  Magnesium–Zinc ferrite nanoparticles, sol-gel auto-combustion method, cubic spinel structure, bond lengths and bond angles, hopping lengths, elastic moduli

FOR CITATION  Patil P.V., Chaudhari N.D., Kute P.R., Kale R.D. Synthesis, investigation, structural and elastic properties of Mg$_x$Zn$_{1-x}$Fe$_2$O$_4$ nanoparticles. *Nanosystems: Phys. Chem. Math.*, 2022, **13** (4), 456–463.

## 1. Introduction

Spinel ferrites are an important magnetic materials for application in different branches of biomedical, ferrofluid, microwave and data storage devices, magnetocaloric refrigeration, gas sensors, etc. due to its electronic, magnetic, and catalytic properties [1]. The promising and extensively used Mg–Zn ferrite nanoparticles are suitable for applications not only in the field of electronics [2], heterogeneous catalysis, sensors, magnetic technologies, but also in medicine for cancer treatment by hyperthermia [3] and other biomedicines [4]. Chemically and thermally stable zinc ferrite material are used for photocatalysis, magnetic resonance imaging (MRI), drug delivery, and pigments [5,6]. Rahaman and Ichiyanagi [7,8] reported that in Mg–Zn ferrite, Mg ferrite has an inverse spinel structure with Mg$^{2+}$ cations mainly on octahedral site while Zn ferrite has a normal spinel structure in which Zn$^{2+}$ occupies the tetrahedral site [7,9]. The cations distribution is mainly dependent on the synthesis technique and ambient conditions [10–12].

To tailor the desired properties of ferrite nanoparticles, various physical and chemical routes are used for synthesizing ferrite materials such as ceramic, co-precipitation, auto-combustion, hydrothermal, citrate precursor, etc. [13]. The preparation of Mg–Zn ferrite nanoparticles [14–16] through the Sol-Gel auto-combustion route has its importance in the area of research and development. Better control over particle size can be possible by combustion route which helps one to improve properties of the materials. Keeping in mind the importance of this synthesis route, the different compositions of Mg–Zn ferrites has been synthesized in the present work and its structural and elastic properties as a function of composition are reported.

## 2. Experimental

The Magnesium Nitrate Mg(NO$_3$)$_2$ · 6H$_2$O, Zinc Nitrate Zn(NO$_3$)$_2$ · 6H$_2$O, Ferric Nitrate Fe(NO$_3$)$_2$ · 6H$_2$O, and citric acid (C$_6$H$_8$O$_7$H$_2$O) are used for preparing the composition of Mg$_x$Zn$_{1-x}$Fe$_2$O$_4$ ferrite for $x = 0.0$, 0.2, 0.6, 0.8, and 1.0. All the metal nitrates are dissolved in distilled water and are mixed with a 1:3 ratio of nitrate to citric acid. By keeping these solutions on the hot plate (90 °C) on the magnetic stirrer, the mixed solutions become viscous and finally formed into a viscous gel. This viscous gel began frothing after evaporating all water molecules' contents and the gel automatically ignited and burned with glowing flints and fully loosed powdered ash remained in the container of the gel. This powdered ash was then sintered (at 1000 °C) for four hours in an automatic temperature-controlled muffle furnace.

The structural characteristics of both of these sintered and non-sintered ferrite powder were studied by FTIR spectrometer (IRAffinity – 1S WL of Shimadzu Corporation, Japan) and powder X-ray diffractometer (BRUKER D8).

## 3. Results and discussion

### 3.1. X-ray diffraction(XRD)

Figures 1 and 2 show the X-ray diffraction patterns for $Mg_xZn_{1-x}Fe_2O_4$ ferrite compositions (both non-sintered and sintered) and confirm the formation of single-phase cubic spinel structure of ferrites. All the compositions also show the characteristics reflections of cubic spinel ferrites and confirm the formation of cubic spinel structure without any signs of the secondary phase. The peaks (222), (311), (222), (400), (422) were indexed using JCPDS. X-ray diffraction patterns clearly show the sintering temperature-dependent increase in peak intensity confirming the crystallinity increase with simultaneous decrease of full width at half maxima (FWHM).
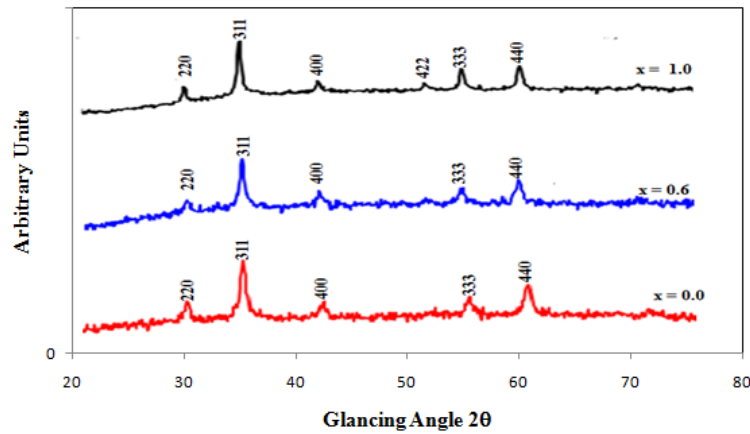


FIG. 1. XRD pattern of non-sintered (as synthesized) $Mg_xZn_{1-x}Fe_2O_4$ ferrite
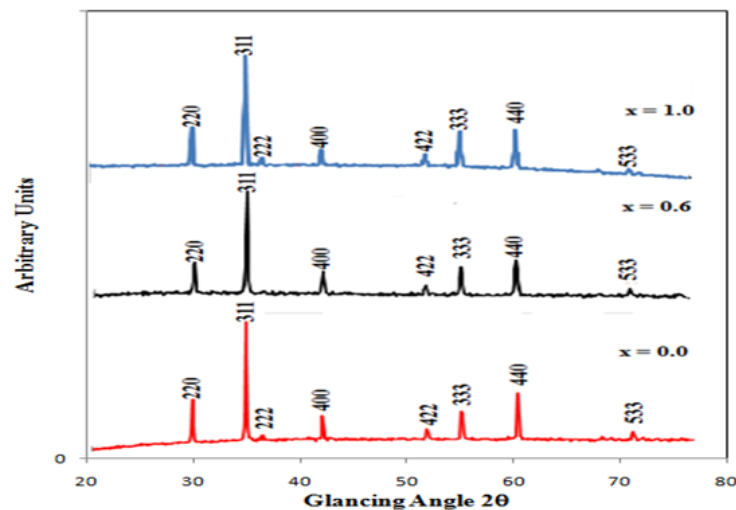


FIG. 2. XRD pattern of sintered $Mg_xZn_{1-x}Fe_2O_4$ ferrite

The broadening of the most prominent peaks (311) of synthesized powder of all compositions is used for the analysis of crystallite size. The Debye–Scherrer formula was used to calculate crystallite size of ferrite nanoparticles, $D_{311} = \dfrac{k\lambda}{\beta\cos\theta}$, where, $k = 0.9$ is a crystallite size constant, $\lambda$ is the wavelength of radiation, $\theta$ is the diffraction angle and $\beta$ is the full width at half maximum (FWHM) of intensity for (311) peak. Experimental lattice parameters were obtained using relation $a_{exp} = d_{hkl}[h^2 + k^2 + l^2]^{1/2}$ while the theoretical lattice parameter [17] was calculated by the following relation:

$$a_{th} = \frac{8}{3}\sqrt{3}\left[(r_A + R_0) + \sqrt{3}\,(r_B + R_0)\right]. \tag{1}$$

Here, $R_0 = 1.38$ Å is the oxygen ion radius, ionic radii of the tetrahedral [A] and the octahedral [B] sites are $r_A$, $r_B$, respectively.

Both these experimental and theoretical lattice parameters for the present ferrite composition are listed in Table 1. The decrease in both the theoretical and experimental values of lattice constant (a) confirms the increase in $Mg^{2+}$ content from 8.441 to 8.349 Å, clearly obeying Vagard's Law [18]. The difference in the ionic radii of replaced and replacing ions causes this abetment, which depicts the linear change in the lattice constant with the substation of different ions. The ionic radii difference of $Mg^{2+}$ (0.65 Å) and $Zn^{2+}$ (0.83 Å) causes the diminution of the lattice constant. Manikandan et al. [1] and Rahman [7] also reported similar results. The X-ray density was calculated by relation $\rho_x = \dfrac{ZM}{Na^3}$ and the bulk density or actual density was obtained by making the pellet of synthesized material, using relation $\rho_a = \dfrac{m}{\pi r^2 h}$. Here $m$ is the mass, $r$ is the radius and $h$ is the thickness of the pellet.

TABLE 1. Lattice Parameter ($a_{exp}$ and $a_{th}$), Crystallite size ($D$), X-ray density ($\rho_x$), actual density ($\rho_a$) [$\pm 0.006$]

| $x$ | $a_{exp}$ (Å) | $a_{th}$ (Å) | $D$ (nm) | $\rho_x$ (gm/cc) | $\rho_a$ (gm/cc) |
|------|------|------|------|------|------|
| 0.00 | 8.349 | 8.441 | 22.6 | 5.325 | 4.635 |
| 0.20 | 8.331 | 8.423 | 23.4 | 5.176 | 4.759 |
| 0.40 | 8.310 | 8.402 | 23.4 | 5.030 | 4.568 |
| 0.60 | 8.302 | 8.394 | 22.8 | 4.860 | 4.237 |
| 0.80 | 8.276 | 8.368 | 23.5 | 4.719 | 4.108 |
| 1.00 | 8.349 | 8.441 | 23.8 | 4.565 | 4.059 |

The bond length ($d_{AX}$, $d_{BX}$) site radii ($r_A$, $r_B$), tetrahedral edge ($d_{XX}$), octahedral edges (shared and unshared) ($d'_{XX}$, $d''_{XX}$), hoping length radii ($L_A$, $L_B$) are calculated by the following relations. The corresponding values are presented in Table 2.

$$d_{AX} = a\sqrt{3}\left(u - \frac{1}{4}\right), \quad d_{BX} = a\sqrt{3u^2 - \frac{11}{4}u + \frac{43}{64}}, \quad d_{XX} = a\sqrt{2}\left(2u - \frac{1}{2}\right),$$
$$d'_{XX} = a\sqrt{2}(1 - 2u), \quad d''_{XX} = a\sqrt{4u^2 - 3u + \frac{11}{16}}, \quad L_A = a\frac{\sqrt{3}}{4}, \quad L_B = a\frac{\sqrt{2}}{4}. \tag{2}$$

TABLE 2. Hopping lengths ($L_A$, $L_B$), bond length ($d_{AX}$, $d_{BX}$), site radii ($r_A$, $r_B$), tetrahedral edge ($d_{XX}$), shared and unshared octahedral edges ($d'_{XX}$, $d''_{XX}$) for present ferrite composition [$\pm 0.0004$]

| $x$ | $L_A$ | $L_B$ | $d_{AX}$ | $d_{BX}$ | $r_A$ | $r_B$ | $d_{XX}$ | $d'_{XX}$ | $d''_{XX}$ |
|------|------|------|------|------|------|------|------|------|------|
| 0.00 | 3.6551 | 2.9843 | 1.8275 | 2.1103 | 0.4475 | 0.7302 | 2.9844 | 2.9843 | 2.9843 |
| 0.20 | 3.6473 | 2.978 | 1.8236 | 2.1058 | 0.4436 | 0.7257 | 2.9779 | 2.978 | 2.978 |
| 0.40 | 3.6382 | 2.9706 | 1.8190 | 2.1005 | 0.4391 | 0.7205 | 2.9705 | 2.9706 | 2.9706 |
| 0.60 | 3.6347 | 2.9677 | 1.8173 | 2.0985 | 0.4374 | 0.7185 | 2.9677 | 2.9677 | 2.9677 |
| 0.80 | 3.6235 | 2.9585 | 1.8117 | 2.0920 | 0.4317 | 0.7120 | 2.9585 | 2.9585 | 2.9585 |
| 1.00 | 3.6152 | 2.9518 | 1.8076 | 2.0873 | 0.4276 | 0.7072 | 2.9518 | 2.9518 | 2.9518 |

The values of all these parameters clearly show the effect of an increase in $Mg^{2+}$ content in the composition which is related to larger values of $Zn^{2+}$ ions as compared to $Mg^{2+}$ ions. This substitution dependent bond length change for tetrahedral and octahedral sites was reported by Vara Prasad et al. [19]. The hopping length behavior may be attributed to the ionic radii difference and causes the decrease in hopping length [20].

The lattice and oxygen parameter variation in terms of cation-cation [Me–Me] and cation-anion [Me–O] bond length and bond angles [21, 22] are obtained using relations. Particularly, cation-cation [Me–Me] bond lengths are as follows :

$$b = \sqrt{2}\frac{a}{4}, \quad c = \sqrt{11}\frac{a}{8}, \quad d = \sqrt{3}\frac{a}{4}, \quad e = \sqrt{3}\frac{3a}{8}, \quad f = \sqrt{6}\frac{a}{4}, \tag{3}$$

cation-anion [Me–O] bond lengths:

$$p = a\left(\frac{5}{8} - u\right), \quad q = a\left(u - \frac{\sqrt{3}}{4}\right), \quad r = a\left(u - \frac{\sqrt{11}}{4}\right), \quad s = a\left(\frac{u}{3} + \frac{1}{8}\right)\sqrt{3}. \quad (4)$$

Here $u = \dfrac{5\sqrt{3}l_A^T + 6l_A^o}{8\left[\sqrt{3}l_A^T + 3l_A^o\right]}$ for normal spinel and $u = \dfrac{5}{8} - \dfrac{9l_A^o}{8\left[\sqrt{3}l_B^T + 3\frac{Z_A l_A^o + Z_B l_B^o}{Z_A + Z_B}\right]}$ for inverse spinel structure [21].

The values of all these parameters in Table 3 show that both these [Me–Me] and [Me–O] bond lengths decreases due to an increase in ions of $Mg^{2+}$ in the composition. The variation in the ionic radii of $Mg^{2+}$ and $Zn^{2+}$ ions and the lattice constant affects the changes in the bond length of all the compositions.

TABLE 3. Cation-cation [Me–Me] and cation-anion [Me–O] bond length for present ferrite composition [$\pm 0.0004$]

| $x$ | cation-cation | | | | | cation-anion | | | |
|---|---|---|---|---|---|---|---|---|---|
| | b | c | d | e | f | p | Q | r | s |
| 0.00 | 2.9843 | 3.4995 | 3.6551 | 5.4825 | 5.1690 | 2.1102 | 1.8275 | 3.4994 | 3.6551 |
| 0.20 | 2.9779 | 3.4920 | 3.6473 | 5.4709 | 5.1580 | 2.1057 | 1.8236 | 3.4919 | 3.6473 |
| 0.40 | 2.9705 | 3.4833 | 3.6382 | 5.4572 | 5.1451 | 2.1005 | 1.8190 | 3.4832 | 3.6382 |
| 0.60 | 2.9677 | 3.4800 | 3.6347 | 5.4520 | 5.1402 | 2.0985 | 1.8173 | 3.4799 | 3.6347 |
| 0.80 | 2.9585 | 3.4692 | 3.6235 | 5.4352 | 5.1243 | 2.0920 | 1.8117 | 3.4691 | 3.6235 |
| 1.00 | 2.9518 | 3.4613 | 3.6152 | 5.4228 | 5.1127 | 2.0872 | 1.8076 | 3.4613 | 3.6152 |

The concentration-dependent bond angles ($\theta_1$, $\theta_2$, $\theta_3$, $\theta_4$, $\theta_5$) shown in Fig. 3 were calculated by trigonometric relations [21] and were found to be 125.25 close to ideal and reported values [23] for all compositions of Ni–Zn ferrite.
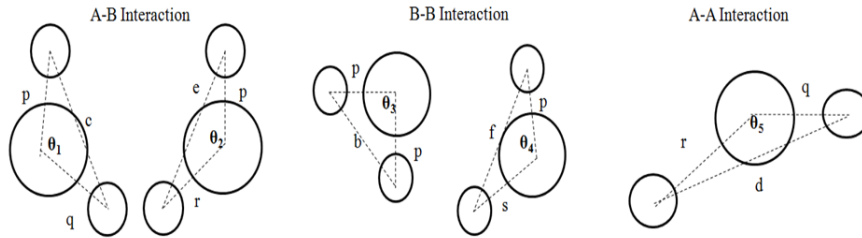


FIG. 3. Spinel structure with bond length and bond angles

$$\theta_1 = \cos^{-1}\left[\frac{(p^2 + q^2 - c^2)}{2pq}\right], \quad \theta_2 = \cos^{-1}\left[\frac{(p^2 + r^2 - c^2)}{2pr}\right], \quad \theta_3 = \cos^{-1}\left[\frac{(2p^2 - b^2)}{2p^2}\right],$$

$$\theta_4 = \cos^{-1}\left[\frac{(p^2 + s^2 - f^2)}{2ps}\right], \quad \theta_5 = \cos^{-1}\left[\frac{(r^2 + q^2 - d^2)}{2rq}\right]. \quad (5)$$

## 3.2. FTIR study

The Fourier transforms IR spectroscopy is useful to determine the crystalline symmetry. It is used for the analysis of spinel structure formation in ferrites. Fig. 4 shows FTIR spectra of sintered ferrite nanoparticles of $Mg_xZn_{1-x}Fe_2O_4$ for $x = 0.0, 0.6, 1.0$ composition.

As shown in the Fig. 4, FTIR spectra for these compositions depict the spinel structure formation of ferrite by absorption dip corresponding to tetrahedral and octahedral vibrational complexes at around $528 - 465$ and $409 - 432$ cm$^{-1}$ respectively. The increase in $Mg^{2+}$ concentration results in the shifting of the wavenumber of band: $\upsilon_1$ shifts towards higher values and $\upsilon_2$ shifts towards lower values. The tetrahedral site is occupied by $Zn^{2+}$ ions with a larger ionic radius which affects the band position. The stretching of tetrahedral ions and oxygen bonding causes absorption band $\nu_1$ while the transverse vibrations of oxygen with tetrahedral sites cause band $\upsilon_2$. Absorption band $\nu_1$ with the intrinsic vibration
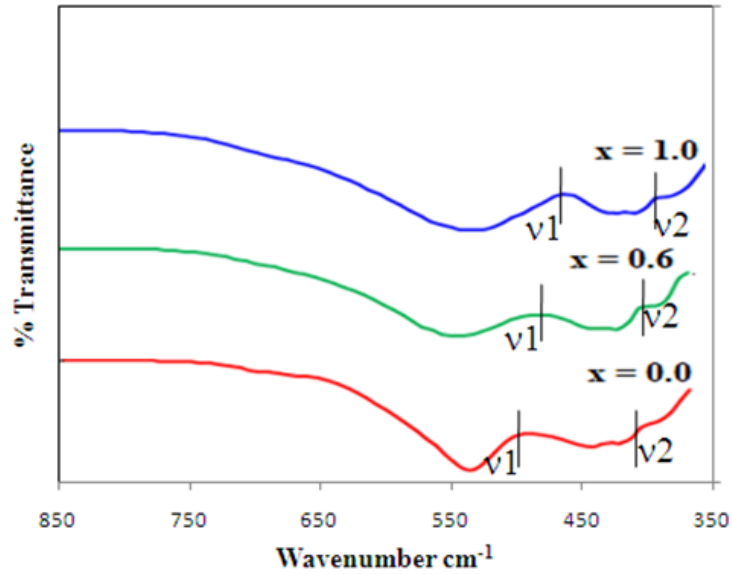
FIG. 4. FTIR spectra for sintered $Mg_xZn_{1-x}Fe_2O_4$ ferrite composition for $x = 0.0, 0.6, 1.0$

of tetrahedral groups corresponds to the restoring force and band $\nu_2$ of octahedral groups corresponds to bond bending vibrations [24].

The difference in $Fe^{3+}$–$O^{2-}$ distance of A and B site also reflects the dissent between the positions of both $\nu_1$, $\nu_2$ bands in FTIR spectra. In the present work, the absorption bands for the present ferrite composition (Mg–Zn) were found close to the reported values. Table 4 shows force constants for the tetrahedral and octahedral sites calculated in [25] using the following formulas, $K_t = 7.62 \times M_1 \times \upsilon_1^2 \times 10^{-7}$ N/m and $K_0 = 10.62 \times \dfrac{M_2}{2} \times \upsilon_2^2 \times 10^{-7}$ N/m, where, $K_t$, $K_0$ are the force constants, $M_1$, $M_2$ are the molecular weights and $\nu_1$, $\nu_2$ are the vibrational bands corresponding to tetrahedral and octahedral sites, respectively.

TABLE 4. Vibrational bands, force constants, longitudinal modulus ($L$), shear modulus ($G$), bulk modulus ($B$), Young modulus ($E$)

| $x$ | $\nu_1$ (cm$^{-1}$) | $\nu_2$ (cm$^{-1}$) | $K_t$ (N/m) | $K_0$ (N/m) | $L$ (GPa) | $G$ (GPa) | $B$ (GPa) | $E$ (GPa) |
|------|------|------|--------|--------|--------|-------|-------|--------|
| 0.00 | 490 | 415 | 136.79 | 110.68 | 146.59 | 48.86 | 81.44 | 122.16 |
| 0.20 | 526 | 426 | 133.82 | 101.55 | 139.70 | 46.57 | 77.62 | 116.42 |
| 0.40 | 526 | 428 | 129.8 | 96.37 | 134.58 | 44.86 | 74.77 | 112.15 |
| 0.60 | 492 | 402 | 128.66 | 82.4 | 125.71 | 41.90 | 69.84 | 104.76 |
| 0.80 | 528 | 412 | 122.68 | 77.93 | 119.85 | 39.95 | 66.59 | 99.88 |
| 1.00 | 465 | 392 | 120.44 | 71.19 | 114.76 | 38.25 | 63.76 | 95.63 |

The force constants values from Table 4 show decrement in force constant $K_0$ and $K_t$ as a function of increasing $Mg^{2+}$ content in all compositions, such that $K_t > K_0$.

The elastic parameter and Debye temperature [24, 26] are calculated here using frequency band relation $\theta_1 = 1.438\upsilon_{av}$, where $\upsilon_{av} = \left(\dfrac{\upsilon_1 + \upsilon_2}{2}\right)$. The Debye temperature variation from 676 to 687 K regulates the heat conduction mechanism in the ferrites. Based on specific heat theory and the heat conduction mechanism, a decrease in Debye temperature with an increase in Mn content in Li–Mn ferrites also was reported in [27].

Debye temperature ($\theta_D$) was calculated using the density of the sample, the molecular weight and the mean wave velocity in accordance with the following relation:

$$\theta_D = \frac{h}{K_B}\left(\frac{3\rho q N_A}{4\pi M}\right)^{1/3} V_m, \tag{6}$$

where $h$ is Planck's constant, $K_B$ is Boltzmann's constant, $N_A$ is Avogadro's number, $M$ is the molecular weight, $q$ is the number of atoms in unit formula, $\rho$ is the density of the sample [28].

The product of the stiffness constant ($C_{11} = L$; Longitudinal modulus) and the lattice constant ($a$) was used to obtain elastic moduli [29] estimation by the force constant ($K = (K_t + K_0)/2$). The pore fraction ($p = 1 - \rho_a/\rho_x$) for each composition was obtained using the corresponding values of the X-ray density ($\rho_x$) and the bulk density ($\rho_a$).

The longitudinal wave velocity ($V_L$) and the transverse wave velocity ($V_T$) [30] were determined by, $V_L = \left( \dfrac{C_{11}}{\rho_x} \right)^{1/2}$ and $V_T = \dfrac{V_L}{\sqrt{3}}$. Similarly, the shear modulus ($G$), the bulk modulus ($B$), the Young modulus ($E$), Poisson's ratio ($\sigma$), the mean wave velocity ($V_m$) [31] are determined using the following relations,

$$G = \rho \times (V_T)^2, \quad B = L - \left( \frac{4}{3} \right) G, \quad E = (1+\sigma)\, 2G, \quad \sigma = \frac{3B - 2G}{6B + 2G}, \quad V_m = \left[ \frac{1}{3} \left( \frac{1}{V_L{}^3} + \frac{2}{V_T{}^3} \right) \right]^{-1/3}. \quad (7)$$

The elastic moduli and the wave velocity values are listed in Table 5. This elastic moduli value depicts the dependence on the $Mg^{2+}$ content due to weaken interatomic bonding. The effect of changes in the interatomic bonding strength on the elastic parameters with $Zn^{2+}$ content in Zn–Co ferrites was reported in works [32, 33].

TABLE 5. The longitudinal wave velocity and the transverse wave velocity, the mean wave velocity ($V_m$), Poisson's ratio ($\sigma \pm 0.06$), the elastic moduli corrected to zero porosity ($E_0, G_0, B_0, L_0, \sigma_0$)

| $x$ | $V_L$ (m/s) | $V_T$ (m/s) | $V_M$ (m/s) | $E_0$ (GPa) | $G_0$ (GPa) | $B_0$ (GPa) | $L_0$ (GPa) | $\sigma$ | $\sigma_0$ |
|---|---|---|---|---|---|---|---|---|---|
| 0.00 | 5623.8 | 3246.9 | 3604.66 | 165.054 | 60.08 | 95.57 | 186.346 | 0.25 | 0.21 |
| 0.20 | 5418.2 | 3128.2 | 3472.89 | 138.84 | 55.28 | 94.79 | 168.49 | 0.25 | 0.25 |
| 0.40 | 5427.9 | 3133.8 | 3479.11 | 137.51 | 54.70 | 94.27 | 167.21 | 0.25 | 0.26 |
| 0.60 | 5447 | 3144.8 | 3491.35 | 141.01 | 55.93 | 98.15 | 172.73 | 0.25 | 0.26 |
| 0.80 | 5401.5 | 3118.6 | 3462.21 | 134.91 | 53.51 | 93.96 | 165.31 | 0.25 | 0.26 |
| 1.00 | 5317.3 | 3069.9 | 3408.2 | 122.98 | 48.85 | 84.95 | 150.09 | 0.25 | 0.26 |

The transverse propagation of energy keeps the particles in vibration mode that results in the collisions. Hence, more energy is needed during the transverse wave propagation than for the longitudinal wave [34].

The Debye temperature is used to determine the mode of vibrations and the rigidity of the ferrite material. From Table 6, it is observed that the Debye temperature obtained from the Waldron equation is greater than that obtained from the Anderson equation. Similar behavior was observed by Mazen and Elsaad [35] for Li–Mn ferrite. Both Debye temperatures show decreasing trend with increasing $Mg^{2+}$ content. According to the theory of specific heat, part heat absorbed by electrons causes a decrease in the Debye temperature ($\theta_D$) [35]. It is suggested that the conduction is due to electron in the synthesized ferrite material.

TABLE 6. Debye temperatures ($\theta_D, \theta_1$), $B_0/G_0$ ratio [$\pm 0.08$]

| $x$ | $\theta_D$ (K) | $\theta_1$ (K) | $B_0/G_0$ |
|---|---|---|---|
| 0.00 | 460.84 | 687.36 | 1.70 |
| 0.20 | 456.79 | 684.48 | 1.71 |
| 0.40 | 456.84 | 685.92 | 1.72 |
| 0.60 | 452.68 | 676.57 | 1.75 |
| 0.80 | 450.07 | 675.86 | 1.75 |
| 1.00 | 447.28 | 676.58 | 1.87 |

These two temperature relations ($\theta_D, \theta_1$) reflect the dependence of $Mg^{2+}$ content. The elastic moduli do not show any significant dependence on porous polycrystalline ferrites by nature [36]. The magnitudes of the elastic moduli corrected to zero porosity are higher than non-corrected to zero porosity.

The Pugh criteria [37], the ratio of the Bulk modulus and the Rigidity modulus $B_0/G_0$, is used to decide ductility and brittleness of synthesized material. The ratio greater than the critical value of 1.75 indicates the ductile nature and the ratio lower than 1.75 indicates the brittle nature. In the present case, the ratio $B_0/G_0$ for all the compositions presented in Table 6 varies between 1.70 and 1.87. It leads to the conclusion that the compositions with $x = 0.60$ and $0.80$ are ductile and the remaining are brittle.

## 4. Conclusions

Compositions of $Mg_xZn_{1-x}Fe_2O_4$ with $x = 0.0$, $0.2$, $0.4$, $0.6$, $0.8$, and $1.0$ were successfully synthesized using sol-gel auto-combustion process. Both the X-ray diffraction and FTIR spectra of non-sintered (as-synthesized) and sintered compositions confirm the formation of cubic spinel structure. The crystallite size lies within the $22 - 24$ nm for all compositions. An increase in $Mg^{2+}$ content shows a decrease in the lattice constant from $8.441$ to $8.349$ Å and verifies Vagard's law. There is a decrease in the structural parameters such as tetrahedral, octahedral bond lengths, cation-cation, cation-anion distances, bond angles, hopping length with the increase in $Mg^{2+}$ content. Two absorption bands of FTIR spectra depict tetrahedral site $524 - 532$ cm$^{-1}$ and octahedral site at $409 - 432$ cm$^{-1}$. Tetrahedral absorption band $v_1$ shifts towards higher values and octahedral absorption band $v_2$ shifts towards lower values when there is an increase of $Mg^{2+}$ concentration. The force constants for tetrahedral and octahedral sites show $Mg^{2+}$ content dependence. FTIR data also depict that the increase in $Mg^{2+}$ content affects the changing of the wave velocity, the elastic constants, and the Debye temperature. All the elastic moduli are corrected to zero porosity. The bulk modulus to the rigidity modulus ratio found to vary between $1.70$ and $1.87$ which leads to the conclusion that the compositions with $x = 0.60$ and $0.80$ are more ductile than their counterparts (brittleness).

## References

[1] Manikandam A., Judith Vijaya J., et al. Optical and magnetic properties of Mg-doped ZnFe2O4 nanoparticles prepared by rapid microwave combustion method. *Superlattices and Microstructures*, 2013, **64**, P. 118–131.

[2] Kopaev A.V., Bushkova V.S. Application of the Electron Theory of Sintering to the Ferrite Systems. *Acta Phys. Pol., A*, 2010, **117**, P. 30–33.

[3] Pulisova P., Kovac J., Voigt A., Raschaman P. Structure and magnetic properties of Co and Ni nano-ferrites prepared by atwo step direct microemulsions synthesis. *J. Magn. Magn. Mat.*, 2013, **341**, P. 93–99.

[4] Rodriguez P.Y.R., Hernandez D.A.C., et al. Structural and magnetic properties of Mg–Zn ferrites prepared by sol-gel method. *J. Magn. Magn. Mat.*, 2017, **427**, P. 268–271.

[5] Koseoglu Y., Baykal A., et al. Synthesis and characterization of ZnFe2O4 magnetic nanoparticles via a PEG-assisted route. *J. Alloys and Comp.*, 2008, **462**, P. 209–213.

[6] Qiu J., Wang C., Gu M. Photocatalytic properties and optical absorption of zinc ferrite nanometer films. *Mater. Sci. Eng. B*, 2004, **112**, P. 1–4.

[7] Rahman S., Nadeem K., et al. Structural and magnetic properties of ZnMg-ferrite nanoparticles prepared using the co-precipitation method. *Ceram. Int.*, 2013, **39**, P. 5235–5239.

[8] Ichiyanagi Y., Kubota M., et al. Magnetic properties of Mg ferrite nanoparticles. *J. Magn. Magn. Mat.*, 2007, **310**, P. 2378–2380.

[9] Thummer K.P., Chhantbar M.C., et al. Localized canted spin behavior in Zn$_X$Mg$_{1.5-X}$Mn$_{0.5}$Fe2O4 spinel ferrite system. *J. Magn. Magn. Mat.*, 2004, **28**, P. 23–30.

[10] Qunnunkad S., Winotal P., Phanichphant S. Cation distribution and magnetic behavior of Mg$_{1-X}$Zn$_X$Fe2O4 ceramics monitored Mossbauer Spectroscopy. *J. Electroceram.*, 2006, **16**, P. 363–368.

[11] Gismelseed A.M., Mohammed K.A., et al. Structure and magnetic properties of Zn$_X$Mg$_{1-X}$Fe2O4 ferrites. *J. Phys. Conf. Ser.*, 2010, **217**, 012138.

[12] Da Silva S.W., Nakagomi F., et al. Effect of Zn content in the structural and magnetic properties of Zn$_X$Mg$_{1-X}$Fe2O4 mixed ferrites monitored by Raman and Mossbauer spectroscopies. *J. Appl. Phys.*, 2010, **107** (9), 09B503.

[13] Ajitanshu Vedrtnam, Kishor Kalauni, Sunil Dubey, Aman Kumar. A comprehensive study on structure, properties, synthesis and characterization of ferrites. *AIMS Materials Science*, 2020, **7** (6), P. 800–835.

[14] Md Atiqur Rahman, Mohammad Tariqul Islam, et al. Synthesis and characterization of Mg–Zn ferrite based flexible microwave composites and its application as SNG metamaterial. *Scientific Reprots*, 2021, **11**, 7654.

[15] Pankaj P. Khirade, Apparao R. Chavan, et al. Tuning of physical properties of multifunctional Mg–Zn spinel ferrite nanocrystals: a comparative investigations manufactured via conventional ceramic versus green approach sol-gel combustion route. *Mater. Res. Express*, 2020, **7**, P. 1–16.

[16] Thomas Dippong, Erika Andrea Levei, Oana Cadar. Recent advances in synthesis and applications of MFe2O4 (M = Co, Cu, Mn, Ni, Zn) Nanoparticles. *Nanomaterials (Basel)*, 2021, **11** (6), 1560.

[17] Kazi Haruum Maria, Choudhary Shamima, Hakim, M.A. Structural transformation and hysteresis behavior of Cu–Zn ferrites. *Inter. Nano. Letters*, 2013, **3**, 42.

[18] Pervaiz E., GulI. H. High frequency response, DC resistivity and magnetic studies of holomium substituted Ni-ferrite: A novel electromagnetic material. *J. Magn. Magn. Mat.*, 2014, **349**, P. 27–34.

[19] Prasad V.B.B.V.S. Cation distribution, structural and electric studies on cadmium substituted nickel zinc ferrites. *Mod. Phys. Lett. B*, 2014, **28** (19), 1450155.

[20] Talanov V.M.. Calculation of structural parameters of spinels. *Phys. Stat. Sol. B*, 1981, **106**, P. 99–106.

[21] Khot V.M., Salunkhe A.B., et al. Low temperature synthesis of Mn$_X$Mg$_{1-X}$Fe2O4 ($x = 0$ –1) nanoparticles: Cation distribution, structural and magnetic properties. *J. Phys. D Appl. Phys.*, 2013, **46**, 055303

[22] Penchal Reddy M., Balkrishna G., et al. Structural, magnetic and electrical properties of NiCuZn ferrites prepared by microwave sintering method suitable for MLCI applications. *J. Physics Chem. Solids*, 2010, **71** (9), P. 1373–1380.

[23] Vara Prasad B.B.V.S., Rajesh Babu B., Siva Ram Prasad M. Structural and dielectric studies of Mg$^{2+}$ substituted Ni–Zn ferrites. *Material Science – Poland*, 2015, **33** (4), P. 806–815.

[24] Waldron R.D. Infrared spectra of ferrites. *Physical Review*, 1955, **99** (6), P. 1727–1735.

[25] Pathak T.K., Buch J.J.U., et al. Infrared spectroscopy and elastic properties of nanocrystalline Mg–Mn ferrites prepared by co-precipitation technique. *J. Nanoscience and Nanotechnology*, 2008, **8**, P. 4181–4187.

[26] Mazen S.A., Zaki H.M., Mansour S.F. Infrared absorption and dielectric properties of Mg–Zn ferrite. *Int. J. Pure and Applied Physics*, 2007, **3** (1), P. 40–48.

[27] Kazi H.M., Choudhary S., Hakim M.A. Structural phase transformation and hysteresis behavior of Cu–Zn ferrites. *Int. Nano. Letters*, 2013, **3** (42), P. 1–10.

[28] Anderson O.L. *Physical Acoustics*, Vol. III, Part B, Academic Press, NY, 1965.

[29] Kakani S.L., Hemrajani C. *Text Book of Solid State Physics*, 3rd Edition, S. Chand and Sons, New Delhi, 1997.

[30] Wooster W.A. Physical properties and atomic arrangements in crystals. *Rep. Prog. Phys.*, 1953, **19**, P. 62–82.

[31] Baldev Raj, V., Rajendran P., Palanichamy. *Science and Technology of Ultrasonics*, Narosa Pub. House, New Delhi, 2004.

[32] Lakhani V.K., Modi K.B. $Al^{3+}$ modified elastic properties of copper ferrite. *Solid State Sci.*, 2010, **12** (12), P. 2134–2143.

[33] Waldron R.D. Infrared spectra of ferrite. *Physical Review*, 1995, **99** (6), P. 1727–1735.

[34] Patil V.G., Shirsath S.E., et al. Effect of zinc substitution on structural and elastic properties of cobalt ferrite. *J. Alloys and Comp.*, 2009, **488**, P. 199–203.

[35] Mazen S.A., Abu-Elsaad N.I. IR spectra, elastic and dielectric properties of Li–Mn ferrite. *Hindawi Research Article*, 2012, 907257.

[36] Hasselmann D.P.N., Fulrath R.M. Effect of small fraction of spherical porosity on elastic moduli of glass. *J. Am. Ceram. Soc.*, 1964, **47**, P. 52–53.

[37] Pugh S.F. Relation between the elastic moduli and the plastic properties of polycrystalline pure metals. *Phil. Mag.*, 1954, **45**, P. 823–843.

*Information about the authors:*

*Pradip V. Patil* – PG Department of Physics and Research Centre, VP's ASC College Baramati (Pune), 413133, India; vpasccphysics@gmail.com

*Nandkishor D. Chaudhari* – Department of Physics and Chemistry, Pratishthan Mahavidyalaya, Paithan (Aurangabad), 431107, India; nk.dchaudhari@gmail.com

*Prabhakar R. Kute* – Department of Physics and Chemistry, Pratishthan Mahavidyalaya, Paithan (Aurangabad), 431107, India; kuteprabhakar@gmail.com

*Rajendra D. Kale* – Department of Physics, Tuljaram Chaturchand College, Baramati (Pune), 413102, India; rajendra_kale@yahoo.com